Electric modulus approach to the analysis of electric relaxation and magnetodielectric effect in reduced graphene oxide–poly(vinyl alcohol) nanocomposite

T. N. Ghosh[1] · A. K. Bhunia[2] · S. S. Pradhan[3] · S. K. Sarkar[3]

Abstract

The polymers poly(vinyl alcohol) (PVA) is used as matrices to synthesize a nanocomposite with reduced graphene oxide (rGO). The structural and optical properties of the rGO and the nanocomposites (rGO–PVA) are studied by XRD, FTIR analysis, FESEM studies, Raman spectroscopy and UV–VIS absorption spectroscopy analysis. Interaction of PVA polymer chains with rGO is confirmed from FTIR study. The bandgap of the PVA and rGO–PVA nanocomposites has been studied from UV–VIS absorption spectrum. The refractive index and optical dielectric constants of PVA, GO, rGO and rGO–PVA nanocomposites have been discussed from optical spectrum analysis. The visual structures of the GO, rGO and rGO–PVA nanocomposites are observed from FESEM study. The electric modulus $M^*(\omega)$ formalism used in the analysis enabled us to distinguish and separate the relaxation processes, dominated by marked conductivity in the $\varepsilon^*(\omega)$ representation. In the ceramics studies, the relaxation times are thermally activated and the dipole process has a clearly non-Debye behaviour. The relaxation process is described with the use of the activation energy of approximately $E_A = 0.12$ eV and the characteristic relaxation time, $\tau_0 = 2.07 \times 10^{-7}$ s. The dielectric property of the nanocomposite (rGO–PVA) is studied in zero magnetic field and in magnetic field (H) up to 1.2 T. From these data, magnetodielectric effects are obtained as the variation of real (ε') and imaginary (ε'') parts of complex dielectric constant with H at some frequencies. In our study at 100 kHz for the increase of H from zero to 1 T ε' decreases by 2.5% in rGO–PVA. This fact is indicative of the interaction between rGO filler particles and PVA polymer chains.

1 Introduction

Graphene, an exceptionally electrical and thermal conductive material, is the initial two-dimensional (2D) atomic crystal isolated and studied by Geim, Novoselov and their partners. Its ascent, status and possibilities, and guide are audited in [1–3]. It is a 2D atomic crystal of sp²-bonded carbon atoms with a honeycomb structure. It has especially high mechanical, electrical, thermal and different properties. As a result of these remarkable properties it

has the capability of numerous applications. The synthesis, properties and utilizations of graphene-based materials belong to a significant zone of research [4–6]. Its one branch is graphene–polymer nanocomposites. Graphene-based materials are blended as nanofillers in polymer frameworks. Inferable from its few remarkable properties, graphene is a handy component as a strengthening material mixed with polymers to support their mechanical properties [7–9] and electrical conductivities [10–12]. Due to the brilliant properties of graphene-based materials the mechanical, thermal, electrical and different properties of the polymer are improved with low substance of the fillers. Stankovich et al. [13] first integrated an electrically conductive graphene-based composite with polystyrene. From that point forward numerous works are right now distributed. Kim et al. [8], Potts et al. [15], Kuilla et al. [16], Cai et al. [17], Verdejo et al. [18], Huang et al. [19], Young et al. [20] and Li et al. [21], Marsden et al. [22] and Hu et al. [23] have checked on the tremendous field of the graphene–polymer nanocomposites. The properties of the

✉ A. K. Bhunia
amitphysics87@gmail.com

1 Department of Electronics, Midnapore College (Autonomous), Midnapore 721101, West Bengal, India

2 Department of Physics, Government General Degree College at Gopiballavpur-II, Jhargram 721517, West Bengal, India

3 Department of Physics, Midnapore College (Autonomous), Midnapore 721101, West Bengal, India

nanocomposites rely upon how well the fillers are scattered in the polymers and the connection between polymer chains and fillers. Other than the preparing strategies, the properties of the fillers and polymers and their morphology, orientation and viewpoint proportion and so on decide the properties. The reviewers [14–23] and references in that ought to be counselled for subtleties. Two significant graphene-based materials are graphene oxide (GO) and reduced graphene oxide (rGO). In the chemical techniques for the production of graphene, [4, 24–27] at first graphite oxide is synthesized from graphite. The graphite oxide is peeled into single layers in water or other solvent by ultrasonication. The single layer is called graphene oxide(GO) in light of the fact that it is graphene layer with four oxygen-containing functional groups epoxides, hydroxyls, carboxyls and carbonyls [28, 29]. GO is an electrical insulator because the sp^2 network of graphene is strongly disrupted where the groups are bonded. To remove the groups the dispersion of GO in water or other solvents is reduced by chemicals like hydrazine, sodium borohydride, ascorbic acid etc. The thermal method of simultaneous exfoliation and reduction can also be applied. On reduction the functional groups are largely removed and the sp^2 network of graphene is restored over most portions of the layer. rGO is an electrical conductor far better than GO by several orders of magnitude. Still the conductivity is less than that of pristine graphene because of the residual groups of rGO. So rGO is not exactly graphene but close to it depending on the degree of reduction.

There are different kinds of graphene-based material, for example, chemically modified GO/rGO. Stankovich et al. [13] had really combined isocyanate-treated GO lastly manufactured rGO–polystyrene composite. It is a typical practice to assign any graphene-based material-polymer composite just as graphene–polymer composite. To be explicit it is smarter to assign the composite as GO–polymer/rGO–polymer like GO–PVA/rGO–PVA.

Support and improvement in mechanical properties of polymer happen for both GO and rGO fillers. Likewise thermal properties are improved by them. But for improved electrical conductivity just conductive fillers like rGO fillers are required. The improved mechanical, thermal and electrical properties for countless polymers have been reported. They are reviewed in [14–20]. In any case, the dielectric properties of GO–polymer/rGO–polymer nanocomposites are reported for just in a couple of studies and not explored in [14–23, 32]. For polymer PVA the works of Mitra et al. [30] and Tantis et al. [31] are on the dielectric properties of nanocomposites. Mitra et al. [30] examined a rGO–PVA nanocomposite and found small magnetodielectric impacts in magnetic field up to 1 T. We have been examining the magnetodielectric properties of

the graphene-polymer nanocomposites. The electric modulus plot shows the usual relaxation behaviour.

Presently, in the current work, we report about the dielectric properties and magnetodielectric effect and electric modulus properties in an rGO–polymer nanocomposite rGO–PVA, rGO content being 2 wt% in the composites. We have estimated the dielectric parameters in zero magnetic field and the magnetic fields up to 1.2 T. The magnetodielectric effects variation ε' and ε'' with the magnetic field at some frequencies are found. Unlike GO–polymer nanocomposite we have found non-zero magnetodielectric effects in rGO–polymer nanocomposites. The results though small are significant with possible application. ε' decreases with magnetic field in rGO–PVA nanocomposites. In this paper, we investigate the electric relaxation properties of the rGO–PVA nanocomposites in a wide temperature range by means of dielectric measurement. The electric modulus formalism is applied to analyse the dielectric data. It is demonstrated that this approach is a very effective and simple method to characterize relaxation properties of the rGO–polymer nanocomposite studied.

2 Experimental

2.1 Sample preparation

There are various techniques for nanocomposite manufacture—solution mixing, melt blending, insitu polymerization, latex technology and so on. We orchestrated the rGO–polymer nanocomposites following the solution mixing method. We initially depict the method for water-dissolvable polymers PVA. Graphite oxide powder prepared by modified Hummers technique [33, 34] was scattered in water and shed by ultrasonication. This dispersion was ultracentrifuged to remove unexfoliated particles. By the repeated use of these two procedures finally a stable aqueous dispersion of graphene oxide (GO) was prepared. The polymer PVA was dissolved in hot water at 90 °C. When the polymer solution was cooled the requisite amounts of the GO dispersion and polymer solution are mixed by constant stirring. Then the requisite amount of hydrazine was added to the mixture and it was stirred constantly overnight. The colour of the mixture turned black but no precipitate was formed. It meant that the GO nanofillers were converted into the rGO nanofillers and remained uniformly dispersed within the polymer matrix. Being surrounded by polymer the rGO fillers were prevented from restacking and aggregation and remain as separated fillers in the polymer matrix. The mixture was poured into petridishes. After the evaporation of water thin films are formed. The thin films of rGO–PVA nanocomposites were peeled off from the petridishes. Salavagione et al. [35] had applied this method to synthesize rGO–PVA

nanocomposites of various concentration of rGO. They found the electrical percolation threshold between 0.5wt% and 1wt%.

2.2 Measurement instruments with set parameters

X-ray diffraction (XRD) patterns were carried out with the apparatus Rigaku Miniflex 600 (Cu target) using CuKα ($\lambda = 1.54°$A) radiation to know the morphological structure of rGO–polymer nanocomposites. The Fourier transform infrared (FT-IR) spectra were collected with a Magna-IR 560 E.S.P spectrometer. FESEM was performed to determine the degree of exfoliation and the quality of the nanofiller dispersion in the nanocomposite. Raman spectra were recorded on a Renishaw inVia confocal Raman microscope system using green (532 nm) laser excitation. The optical spectra of the prepared samples were recorded by using Shimadzu-Pharmaspec-1700 UV–VIS spectrometer with wavelength range 200 nm to 70 nm after ultrasonication of the samples in the solvent water. The dielectric properties and electric modulus were measured by the LCR meter (HIOKI 3536 LCR METER) (frequency range 1 Hz–300 kHz) with zero magnetic field and with magnetic field (H) upto 1.2 T. How the sample was placed in the gap between two pole pieces of the electromagnet with gap (d) 0.5 cm is shown in Fig. 1, the schematic diagram of experimental set-up.
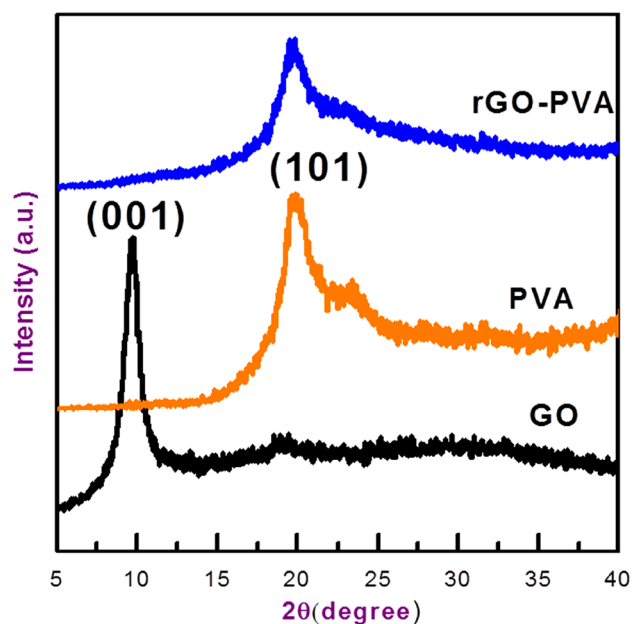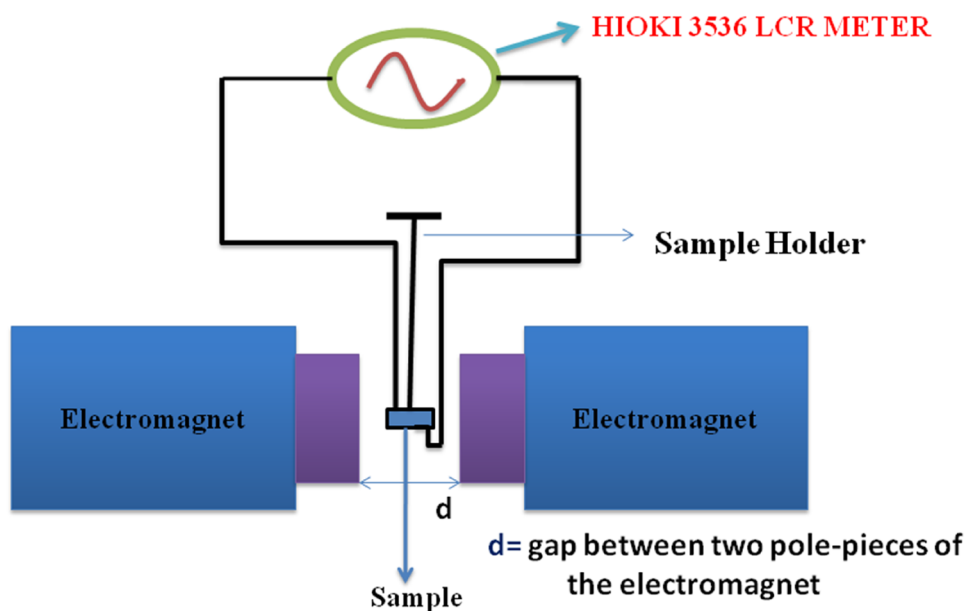

Fig. 2 XRD pattern of GO, PVA, and rGO–PVA Nanocomposites

3 Results and discussion

3.1 XRD studies of the nanocomposites

The XRD pattern of GO, PVA and rGO–PVA Nanocomposites is shown in Fig. 2. The most prominent and unique peak of GO is observed around $2\theta = 10°$ corresponding (001) plane diffraction [36]. From the figure it is seen that no peak of graphite oxide is present in the nanocomposite

Fig. 1 Schematic diagram of the experimental set-up

diagrams. It indicates that rGO is uniformly dispersed into the PVA polymer matrix. The diffraction of PVA peak arises at $2\theta = 19.9°$ corresponding to (101) plane [37]. Further the main peak of PVA at $2\theta = 19.9°$ (in Fig. 2) was slightly shifted to lower $2\theta = 19.2°$ in rGO–PVA and it is also broadened. It means that some interaction between polymer chains and rGO particles had occurred due to dispersion and exfoliation of rGO nanosheets into PVA matrix with somewhat disorder and loss in its structural regularity. Meanwhile, the crystalline structure of PVA was slightly affected by the incorporation of rGO.

3.2 FT-IR studies of the nanocomposites

Figure 3 shows the FT-IR spectra of graphite, GO, rGO, PVA and the rGO–PVA nanocomposite. Within the spectrum of GO the presence of various oxygen-containing groups on the GO surface was confirmed by peaks at 3430 cm^{-1} due to O–H stretching vibration of carboxyl groups and also the absorbed water. The peaks at 1385 and 1270 cm^{-1} correspond to the skeletal vibrations of C–OH and C–O–C. The peak at 1630 cm^{-1} corresponds to C=C skeletal stretching vibration. The characteristic peak for C=O stretching vibration appears at 1730 cm^{-1}, respectively [25, 38, 39]. After solvothermal treatment of GO colloidal dispersions, the partial reduction of GO to rGO is conclusive, based on the significant attenuation of O–H bond peak intensity at 3430 cm^{-1} and therefore the disappearance of C=O bond peak at 1730 cm^{-1}. However, other peaks from C–OH and
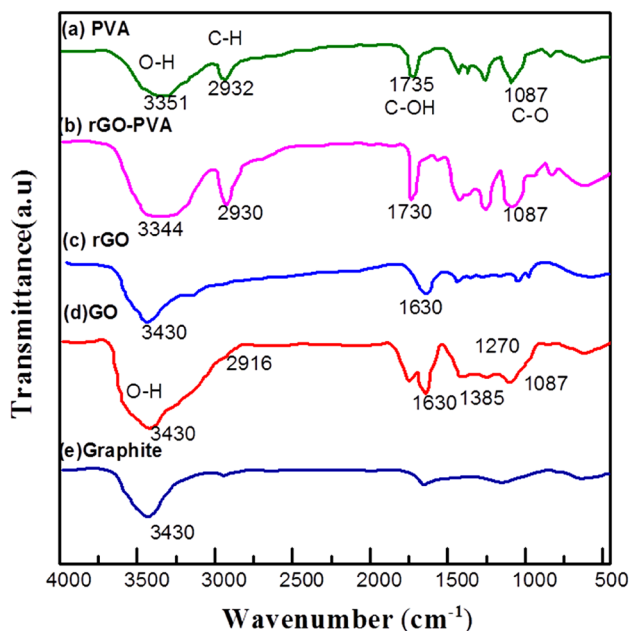
C–O bonds remain almost unchanged, which indicates that the obtained rGO still remains some oxygenated functionalities. Advantageously, the residual oxygenated functionalities can generate strong interactions with the PVA matrix mainly by hydrogen bonds [35, 40, 41]. From the spectra of PVA and rGO/PVA nanofillers, we are able to see that there is absorption peak between 3000 cm^{-1} and 3500 cm^{-1}, which is that the O–H stretching, indicating the existence of strong intermolecular and intramolecular hydrogen bonding [42]. The shift of the peak from 3351 cm^{-1} (pure PVA) to 3344 cm^{-1} for 2 wt% rGO–PVA nanocomposites is attributed to the increase and stronger hydrogen bonding interaction exists between the oxygen-containing functional groups (carboxyl, five membered ring lactols, and hydroxyl on both the basal plane and the edge hydroxyls) of GO and therefore the hydroxyl groups on the PVA molecular chains and also with increase in GO doping concentration also lead to increase in the formation of CTC with OH groups of PVA matrix. Moreover, within the FT-IR spectra of GO and PVA, a stretching vibration band at 2800–3000 cm^{-1} belonging to C–H$_2$ and the peak at 1090 cm^{-1} resulting from the stretching of C–O groups are observed. The change of –OH stretching bands is associated to hydrogen bonding [35, 41, 43, 44]. When rGO was incorporated into PVA, the quality of stretching vibration band at 2800–3000 cm^{-1} becomes stronger. The nanofillers also show a deformation vibration band at 1300–1500 cm^{-1} (CH/CH$_2$ deformation vibrations). From Fig. 3, it can be found that the peak for –OH stretching shifts to a lower wavenumber with the increase of rGO loadings; the band corresponding to –C–OH stretching (around 1095 cm^{-1}) displays an analogous behaviour. In the mean time, the extending vibration of C=O shifts to 1730 cm^{-1}, showing up with higher force inside the rGO–PVA range, demonstrating that hydrogen bond among C=O and OH has been set up.

These phenomena indicate the existence of hydrogen bonding between the hydroxyl groups in PVA and therefore the remaining oxygen-containing functional groups in rGO [45, 46]. The results indicate that there are strong molecular interactions between rGO nanosheets and PVA chains. The strong molecular interactions at the filler–matrix interface are mainly attributed to the hydrogen bonding between the oxygenated groups remaining in rGO surface and the –OH groups of PVA chains [47].

3.3 FESEM studies of the nanocomposite

In order to determine the degree of exfoliation and the quality of the nano rGO dispersion in PVA, scanning electron microscopy (SEM) was employed. Figure 4 shows the SEM images of the GO, rGO and fracture surface of 2 wt% rGO–PVA nanocomposites. The FESEM of the rGO (Fig. 4b clearly indicates the formation of fine nano flakes
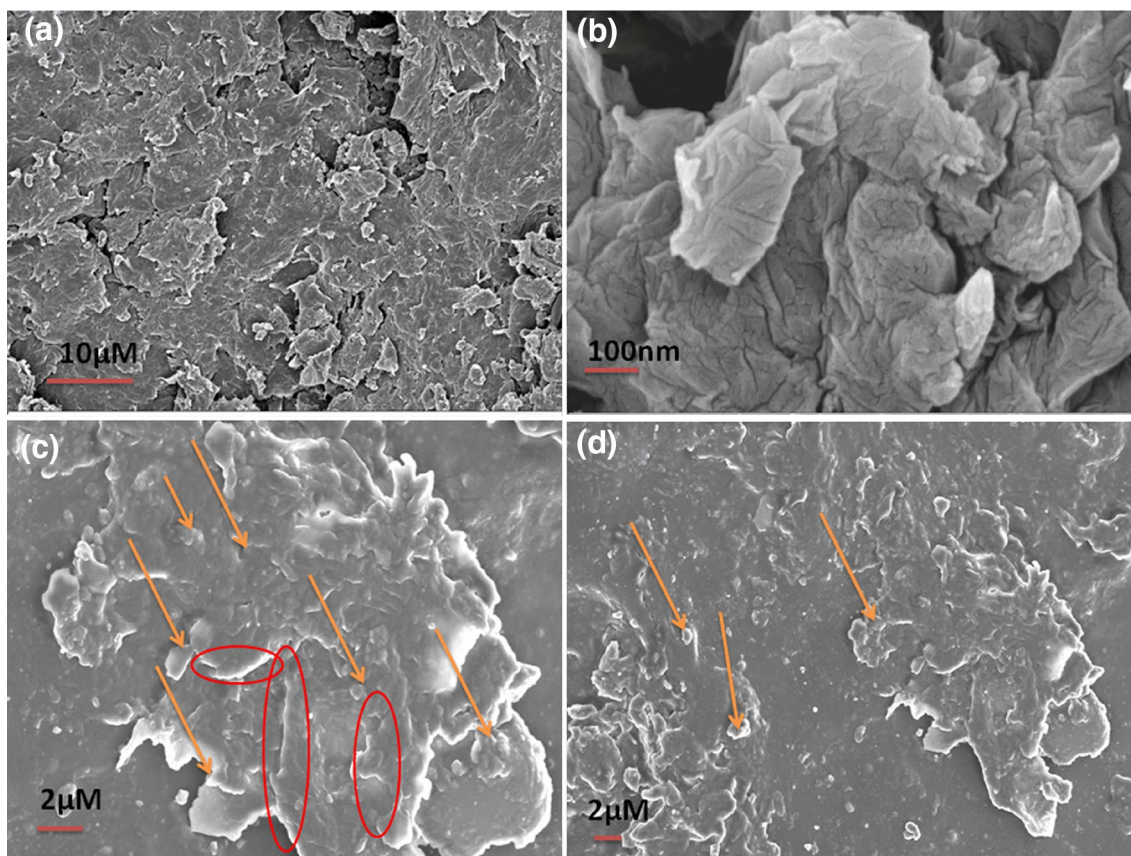
Fig. 3 FT-IR spectra of (a) PVA, (b) rGO–PVA nanocomposite, (c) rGO, (d) GO, (e) graphite

Fig. 4 SEM (FESEM) image of the **a** GO; **b** rGO; **c** rGO–PVA nanocomposites; **d** rGO–PVA nanocomposites
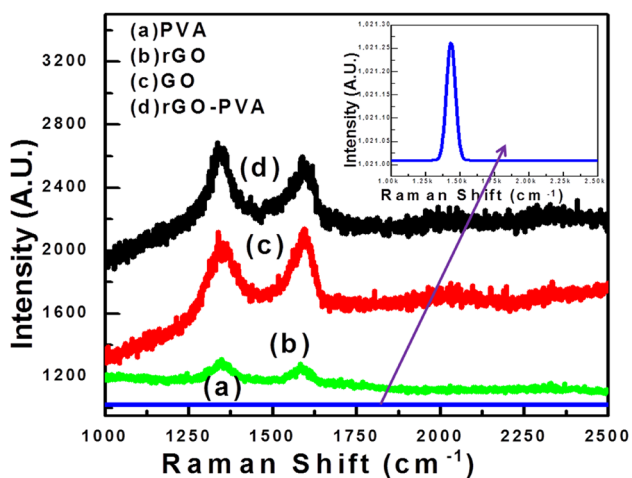

Fig. 5 Raman spectra of graphite, GO, PVA and the rGO–PVA nano-fillers. Inset is the zoom of the PVA Raman spectrum

with smooth surfaces. The FESEM diagram of the nano-composite (rGO–PVA) is given in Fig. 4c, d. It is seen that nano flakes of rGO are well dispersed inside PVA matrix. The evolution of agglomerated sheets is evident for nano-composites of rGO–PVA. Many wrinkles are formed within the composite and rGO nano flakes are penetrated inside PVA polymer chains are marked by red circles in Fig. 4c and arrow sign in Fig. 4c, d, respectively. The wrinkles are formed due to stress and stain inside PVA polymer chains.

3.4 Raman spectroscopy studies of the nanocomposite

Figure 5 shows the Raman spectra of pure PVA, rGO, GO and rGO–PVA nanocomposite. For pure PVA the intensity of the Raman signal is almost constant with respect to the intensity of rGO, GO, rGO–PVA nanocomposites. However, the amplified image (Inset of Fig. 5) of the pure PVA shows a small signal peak around 1430 cm^{-1} inside the scope of 1000 cm^{-1}–2500 cm^{-1} [48]. The zoom of the PVA Raman spectrum is shown in the inset of Fig. 5. By examination, the characteristic peaks at 1345.5 and 1592.7 cm^{-1} show up, relating to D band and G band for GO. The characteristics peaks for rGO arise at 1348.5 and 1598.83 cm^{-1}, relating to D and G bands, respectively. For rGO–PVA nanocomposites, D and G groups are situated at 1354.5 and 1597.75 cm^{-1}, individually. The power proportion of the D band to the G band for rGO and rGO–PVA is 2.25 and 2.01, respectively. This proportion for GO and rGO–PVA is 1.51 and 1.21,

respectively. The correction of D/G proportion recommends the age of a bigger number of sp^2 carbon spaces with a littler normal size in rGO–PVA [49]. We additionally found that the area of D and G bands moved to bring upper wave number compared to GO and rGO. The explanation of area of D and G moved towards higher Raman shift i.e. orginal wavenumber to higher wavenumber possibly is the recuperation of the hexagonal system of carbon particle.

3.5 UV–Visible absorption spectroscopy

Figure 6 represents the UV–Visible absorption spectra for pure GO, rGO, PVA, and PVA–rGO composite films with 2 wt% loading of rGO. Figure 6a shows absorption spectrum of pure PVA. Pure PVA exhibits long-tailed absorption edge around 211.67 nm assigned to n-π* transitions followed by small absorption peak at 273.7 nm which corresponds to $\pi \rightarrow \pi$* transition of carbonyl group of PVA polymer [50]. The maximum absorption of GO arises at 234.5 nm due to plasmon $\pi \rightarrow \pi$* transition with a small peak at 304.45 nm due to n-π* transition shown in Fig. 4c [51]. The maximum absorption of rGO exhibits peak at 273.7 nm shown in Fig. 4c. The reduction of GO leads to the restoration of the sp^2 hybridization carbon atoms within rGO and increase of electron concentration exhibits new absorption peak for rGO [52].

However, in composite samples, the characteristic peak of rGO around 273.7 nm starts disappearing and it shows a new strong absorption at 255.91 nm. The intensity of this characteristic absorption peak within the composite system increases along with large blue shifting with respect to rGO. The large blue shifting in peak clearly indicates the formation of bonding between rGO layers and PVA polymer chains.
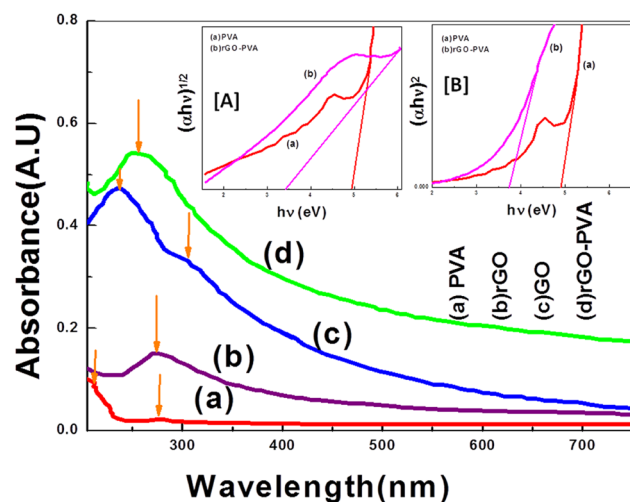
We calculate the bandgap of the pure PVA and rGO–PVA nanocomposite by considering direct bandgap treatment. Optical absorption coefficient has been calculated in the wavelength region 205–750 nm. The bandgap of the PVA and rGO–PVA nanocomposites are determined from the relation: $(\alpha h\upsilon)^n = c(h\upsilon - E_g)$, where c is a constant, E_g is the bandgap of the material, α is the absorption coefficient, factor $n = 2$ for direct bandgap materials and $n = 1/2$ for indirect bandgap materials [53, 54]. Inset [A] & [B] of Fig. 6 shows the plot of $(\alpha h\upsilon)^{1/2}$ vs. energy ($h\upsilon$) & $(\alpha h\upsilon)^2$ vs. $h\upsilon$, respectively, and it is used to determine bandgap [55]. The bandgap (indirect bandgap) of the PVA and rGO–PVA composites are found to be 4.95 eV and 3.35 eV, respectively. The direct bandgap of the PVA and rGO–PVA composites are found to be 4.92 eV and 3.8 eV, respectively [56].

3.6 Refractive index and optical dielectric constants study from UV–Visible absorption spectrum

The refractive index (n) of the material is calculated from reflectance (R) and extinction coefficient (K) of the material by using the following formula [57, 58].

$$n = [(1 + R)/(1 - R)] + \sqrt{[\{4R/(1 - R)^2\} - K^2]},$$

where $K = \alpha\lambda/4\pi t$ and $R = 1 - (A + T)$, A = absorption, T = transmittance, λ is the wavelength and t is the sample thickness. The T values are calculated from Beer's law [54, 59].

The variation of refractive index (RI) as a function of wavelength of pure PVA, rGO, GO, rGO–PVA composites is shown in Fig. 7b. It is clear that the RI of PVA < rGO < GO < rGO–PVA. The results of RI (n) reveal that the incorporation of rGO into PVA polymer matrix can tune the refractive index of the composite material and therefore increase the n value from 1.28 to about 2.49 at $\lambda = 500$ nm. The plot of the extinction coefficient (K) as a function of wavelengths is shown in Fig. 7a. It can be seen that the K value of the rGO–PVA composites is larger than pure PVA and pure rGO at any wavelengths.

The optical dielectric functions (ε_1', ε_1'') are likewise concentrated by optical spectroscopy which are helpful in the assurance of the overall band structure of the material. Refractive index (n) and dielectric constant are two helpful parameters utilized for characterizing the optical properties of materials [60]. From the got estimations of n and K, we can just figure the optical dielectric parameters (ε_1', ε_1'') using the following relations [60]:

Optical dielectric constant $\left(\varepsilon_1'\right) = n^2 - K^2$

Optical dielectric loss $\left(\varepsilon_1''\right) = 2nK$

Fig. 6 UV–VIS spectra of **a** PVA; **b** rGO; **c** GO; **d** rGO–PVA nanocomposite; Inset [A] is the plot of $(\alpha h\upsilon)^{1/2}$ vs. energy ($h\upsilon$); Inset [B] is the plot of $(\alpha h\upsilon)^2$ vs. energy ($h\upsilon$)
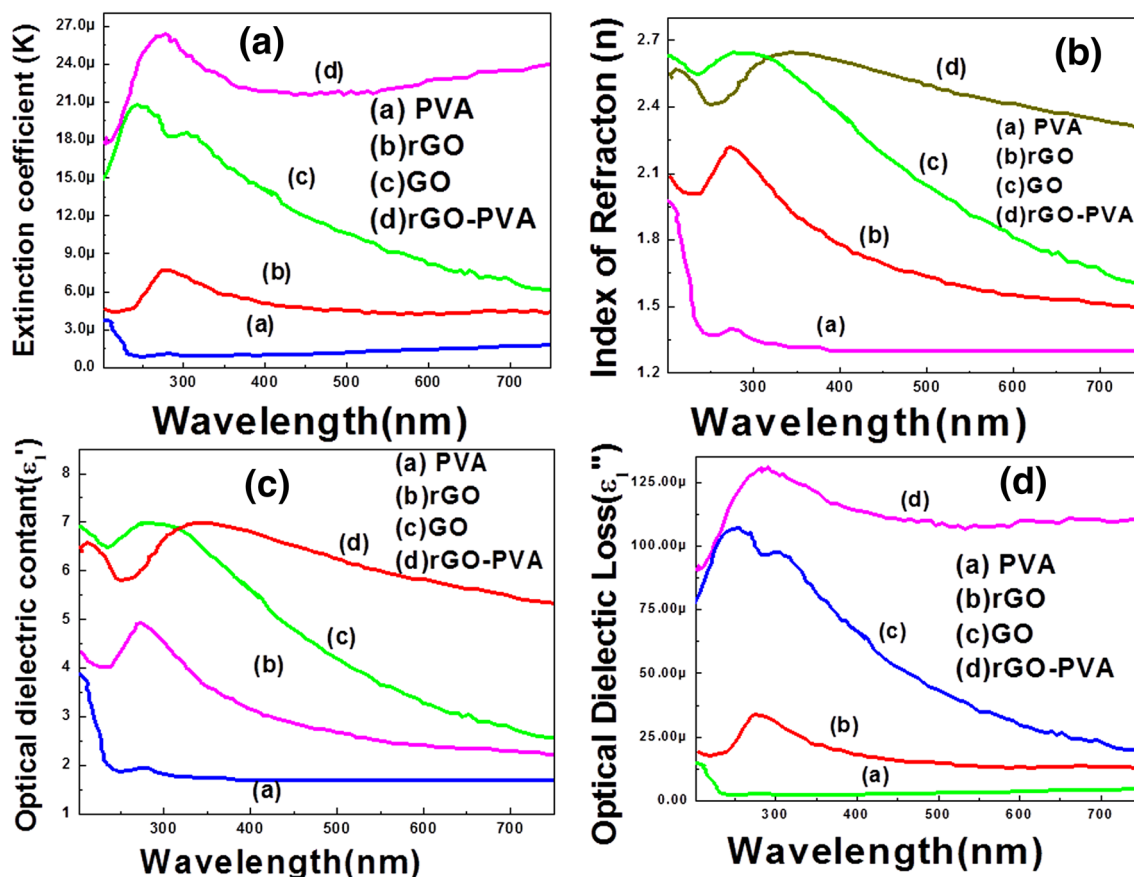
Fig. 7 The variation of **a** Extinction coefficient (K) vs. wavelength (λ); **b** Refractive index (n) vs. λ; **c** Optical dielectric constant (ε_1') vs. λ; **d** Optical dielectric losses (ε_1'') vs. λ of (a) PVA, (b) rGO, (c) GO, (d) rGO–PVA nanocomposite

Figure 7c shows the variation of ε_1' with wavelength for all the samples. It trends to be seen that at higher wavelengths the optical dielectric constants are practically steady for PVA, rGO, rGO–PVA. In case of GO it slightly decreases with increase in wavelength. The real part of the optical complex dielectric constant shows how much it will slow down the speed of light in the material, and is straightforwardly identified with the refractive index ($n \approx \sqrt{\varepsilon_1'}$). Figure 7d represents the variation of ε_2'' with wavelength (λ) and corresponding energy (ε) = hc/λ for pure PVA, GO, rGO, rGO–PVA composite samples. It is clear that at low photon energy i.e. high λ the PVA, rGO, rGO–PVA samples display practically constant estimation of ε_1''. In case of GO, ε_1'' slightly diminishes with increase in wavelength. The imaginary part relates to the absorption coefficient [60, 61]. It was accounted for that the imaginary component of the dielectric function (ε_1''), predominantly portrays the electron transition from the occupied states to unoccupied states [62]. The process of transition of electrons between the bands of a solid is well known by interband absorption process. The absorption edge is brought about by the onset of optical transitions across the fundamental bandgap of a material.

3.7 Dielectric measurement and electric modulus

We took the rGO–*PVA* thin films of square shape of area A and thickness d. The dielectric properties of a medium under alternating electric field of angular frequency ω are described by frequency-dependent complex dielectric constant.

$$\varepsilon^*(\omega) = \varepsilon'(\omega) - i\varepsilon''(\omega),$$

where $i = \sqrt{-1}, \omega = 2\pi f, f$ = frequency $\varepsilon'(\omega)$ = real part of ε^* $\varepsilon''(\omega)$ = imaginary part of ε^*.

The polarization lags behind the field by the frequency-dependent phase $\delta(\omega)$. Then

$$\tan\delta = \frac{\varepsilon''}{\varepsilon'} \tag{1}$$

From measurement

$$\varepsilon' = \frac{C}{C_0} \tag{2}$$

where C_0 = capacitance of the empty capacitor = $\varepsilon_0 \frac{A}{d}$, ε_0 = vacuum permittivity = 8.85×10^{-12} Fm^{-1}, C = capacitance of the film capacitor.

The ac conductivity is given by

$$\sigma_{ac} = \omega \varepsilon_0 \varepsilon'' \tag{3}$$

Electric modulus compares to the unwinding of the electric field in the material when the electric dislodging stays steady. The electric modulus approach started when the proportional complex permittivity was talked about as an electrical analogue to the mechanical shear modulus [63].

From the physical perspective, the electrical modulus identifies with the loosening up of the electric field in the material when the electric displacement remains constant. Consequently, the modulus speaks to the genuine dielectric relaxation process [64–66].

The complex modulus $M^*(\omega)$ was introduced to describe the dielectric response of non-conducting materials. This formalism has been applied similarly to materials with non-zero conductivity. The convenience of the modulus portrayal in the investigation of unwinding properties was exhibited both for vitreous ionic conductors [67] and polycrystalline ceramics [68].

$M^*(\omega)$ could be expressed as Fourier transform of a relaxation function $\varphi(t)$ [67, 69]

$$M^*(\omega) = \frac{1}{\varepsilon^*} = M'(\omega) + iM''(\omega) = M_\infty \left[1 - \int_0^\infty e^{-i\omega t} \left\{ \frac{d\varphi(t)}{dt} \right\} dt \right] \tag{4}$$

where the function $\varphi(t) = \exp\left[-\left(t/\tau_M \right)^\beta \right]$ represents time evolution of the electric field within the material [70] where $\beta (0 < \beta < 1)$ is the stretched exponent and τ_M is the conductivity relaxation time. This function $\varphi(t)$ gives the time evolution of the electric field within the dielectrics:

$$M'(\omega) = \frac{\varepsilon'(\omega)}{\varepsilon'(\omega)^2 + \varepsilon''(\omega)^2}$$
$$M''(\omega) = \frac{\varepsilon''(\omega)}{\varepsilon'(\omega)^2 + \varepsilon''(\omega)^2} \tag{5}$$

Based on Eq. (5) we have changed the form of presentation of the dielectric data from $\varepsilon'(\omega)$ and $\varepsilon''(\omega)$ to $M'(\omega)$ and $M''(\omega)$. The dielectric parameters were obtained from the data measured by the LCR meter using Eqs. (1), (2) and (3). In our experiments, we had measured the dielectric parameters of the 2wt% rGO–PVA nanocomposites in zero magnetic field for the entire frequency range upto 1.5 MHz.

The variation of the real part of the dielectric constant (ε') and imaginary part of the dielectric constant (ε'') with frequency under four different temperatures (30°, 50°, 70°, 90°, 110 °C) are shown in Fig. 8a, b, respectively. Both dielectric constants decrease with increase of frequency upto 1.5 MHz for a particular temperature. The value of the real and imaginary part of the dielectric constants increase with increase of the temperature for any particular frequency.

The variety of imaginary part of electric modulus M″ and real part of electric modulus M′ versus frequency for the rGO–PVA nanocomposite at different temperatures are delineated in Fig. 9a, b, respectively, using Eq. (5).

It is clearly seen that M′ values are low at low frequency and increases with increase in frequency and almost constant with the rise of higher frequencies. In the low-frequency region the values of M' decrease with increase in temperature and the high-frequency side, on expanding temperature the M′ bends rise representing the non-existence of electrode polarization effect in the rGO–PVA nanocomposite. In the high-frequency region, M′ values are merged at all temperatures. The variation of M″ with frequency shows the appearance of a peak at a particular frequency. This unwinding top will in general move of M″

Fig. 8 The variation of the **a** real part of the dielectric constant (ε') and **b** imaginary part of the dielectric constant (ε'') with frequency of rGO–PVA nanocomposite under five different temperatures (30 °C, 50 °C, 70 °C, 90 °C, 110 °C)
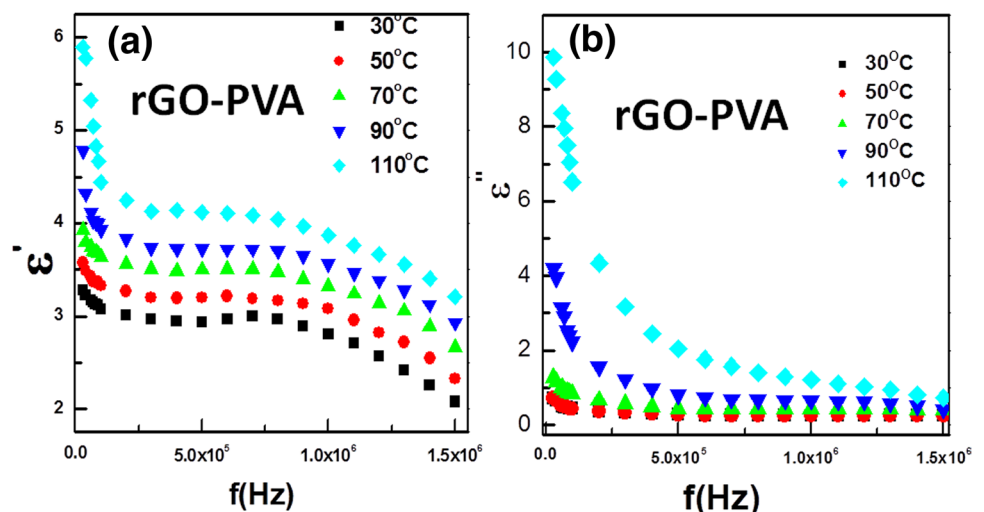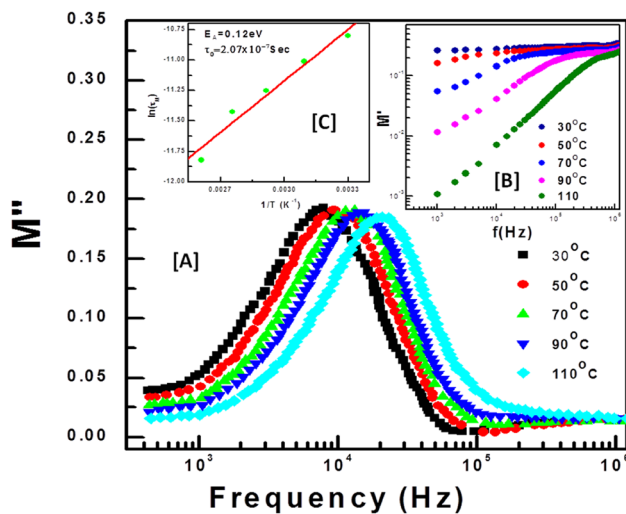
Fig. 9 **A** Frequency dependence of the imaginary component of the electric modulus at temperatures from 30 to110 °C at an interval of 20 °C; **B** Frequency dependence of the imaginary component of the electric modulus at temperatures from 30 to 110 °C at an interval of 20 °C; **C** Electric modulus vs. 1/T for rGO–PVA nanocomposite

Fig. 10 Scaling of the electric modulus $M''(\omega)$ for rGO–PVA nanocomposite sample at different temperatures

towards higher frequencies with expanding temperature. This temperature subordinate conduct of M″ can be clarified on the premise that the charge transporters get thermally enacted with an expansion in the temperature and thus they secure a quick development. This prompts a reduction in the relaxation time and hence increases the relaxation frequency. This causes the shifting of the relaxation peak towards higher frequency with an increase in the temperature and thus signifying the occurrence of temperature-dependent relaxation processes in rGO–PVA nanocomposite. The frequencies at which the peaks in M″ spectroscopic plots are observed follow the relation $\omega_{max}\tau_M = 1$ or $\tau_M = \frac{1}{2\pi f_{max}}$, where ω_{max} is the angular frequency corresponding to the peak maximum. It is seen in Fig. 9a that these relaxation times satisfy an almost linear dependence and hence typically observed that τ_M follows the Arrhenius law given by [71],

$$\tau_M = \tau_0 \exp\left(\frac{E_A}{kT}\right), \tag{6}$$

where E_A the activation energy and τ_0 is the pre-exponential factor. By fitting ln (τ_M) with (1/T) (see Fig. 9c), we find τ_0 and E_A. The values determined from the resultant fitting are $E_A = 0.12$ eV and $\tau_0 = 2.07 \times 10^{-7}$ s, respectively.

Scaling of the electric modulus can give further information about the dependence of the relaxation dynamics on the temperature. Figure 10 shows the scaling results at different temperatures for the rGO–PVA nanocomposite, where M''_{max} and ω_{max} are used as the scaling parameters
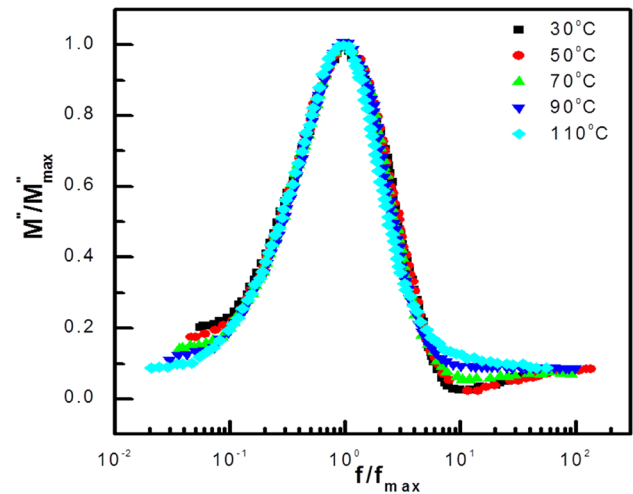
for M″ and ω, respectively. Plainly all modulus spectra can be seen to totally overlap and are scaled to a single master curve showing that the relaxation dynamics does not change with temperature.

3.8 Magnetodielectric effect

With magnetic fields (H) upto 1.2 T in which the film capacitor was placed the frequency scan of the dielectric parameters were obtained. From these measurements, the variation of ε' and ε'' with H at some fixed frequencies were obtained. They are shown in Fig. 11a, b. At a frequency of 100 kHz the increase of H from 0 to 1 T ε' decreases 2.5% for rGO–PVA. Already S. Mitra et al. [30] had studied the 1 wt% rGO–PVA and obtained 1.8% magnetodielectric effect. The magnetodielectric effect is frequency dependent being higher at low frequency. It is better to estimate the magnetodielectric effect, at very high frequencies. As GO is a insulator, GO–polymer nanocomposites do not show magnetodielectric impact as was noted in the introduction. But in some cases, rGO is a conductor. So the interfacial charge in rGO–polymer nanocomposites move under the activity of electric field and magnetic field. The measure of interfacial charges may increase or decrease causing more or less interfacial polarization in magnetic fields. The dielectric parameters ε' and ε'' change with magnetic field (H). We have discovered that ε' decreases with H for rGO–PVA nanocomposite. The works by Mitra et al. [30] discovered magnetodielectric effect in rGO–PVA nanocomposite ε' and ε'' decreases with H. Our film shows a decrease by 2.5% for increment of H to 1 T at 100 kHz. So the comprehension is commonly fantastic with the outcome of Mitra et al. Mitra et al. [30] had applied the theory of magnetocapacitance in non-magnetic composite media by Parish et al. [72] and

Fig. 11 Variation of **a** ε' and **b** ε'' with magnetic field H(G) for rGO–PVA(2 wt%) nanocomposites at constant frequencies: (i) 40 kHz (ii) 50 kHz (iii) 60 kHz (iv) 70 kHz (v) 80 kHz (vi) 90 kHz (vii) 100 kHz
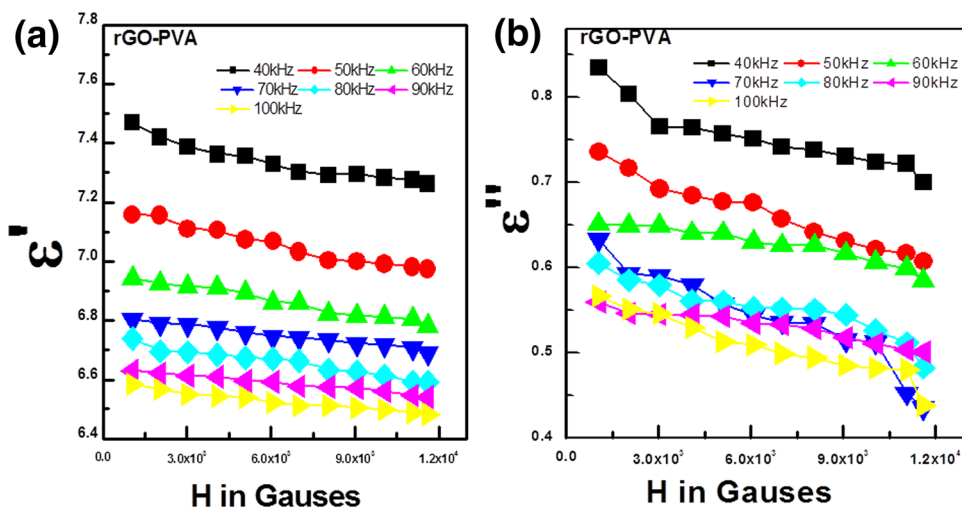
fitted a formula to their ε' and ε'' data. Actually the formula holds only when wt% of rGO = wt% of polymer = 50%, and the system is truly two-dimensional (H applied normal to the plane of the composite). The theoretical work by Catalan [73] on magnetocapacitance without magnetoelectric coupling might be applied if the conductive fillers have magnetoresistance and the composite has MSW effect. We have measured the magnetoresistance of rGO and found it small. So the use of the two hypotheses [72] and [73] are not attempted by us. Further we have found that $\varepsilon', \varepsilon''$, M' and M'' of the nanocomposites in non-zero H do not rely upon the relative orientations of electric field and H. It implies that the nanofillers in our samples are three dimensionally consistently scattered in spherically symmetric style.

From the magnetic field reliance of the dielectric permittivity of this material one will be enticed to utilize it to test magnetic field. Anyway the impact is honestly very little for such an application to be feasible. Use as a magnetic sensor in nanocircuits could still be a chance. Then again, such materials ought to be investigated for making nanogenerators viz; by applying a alternating magnetic field a sinusoidal variety of polarization (for example bound charge density at electrodes)) could be affected.

Recently, Xia et al. [74, 75] had introduced another successful medium theory for the dielectric constant of graphene-based nanocomposites that is gotten from the basic physical procedure including the effects of graphene orientation, aspect ratio, fillers loading, percolation threshold, interfacial tunnelling and Maxwell–Wagner–Sillars polarization [76]. Incidentally there is a theoretical work of Santos et al. [77] which gives the electric field subordinate dielectric steady of unadulterated graphene as ∼ 3.0 for electric field perpendicular to the plane of graphene and 1.8 for the electric field in the plane of graphene. However, the experimental work of Sarkar et al. [78] had reported $\varepsilon' \approx 10^9$ at 20 Hz (colossal dielectricity) due to interfaces and defects. A high $\varepsilon' \approx 10^3$ at 50 Hz for rGO had been reported by Hong et al. [79].

4 Conclusion

The composite formation is clearly observed from Raman spectroscopy analysis and the FESEM study, which shows that nano flakes of rGO are well dispersed inside PVA matrix. The strong interaction between rGO nanosheets and PVA polymer chains is clearly observed from our FTIR analysis. The direct bandgap of the PVA and rGO–PVA composites are found to be 4.92 eV and 3.8 eV, respectively. The results of RI (n) shows that the incorporation of rGO into PVA polymer matrix can increase the refractive index of the composite material from 1.28 to about 2.49 at $\lambda = 500$ nm. We successfully discussed the wavelength-dependent refractive index and optical dielectric constants. We have investigated the electric modulus approach to the analysis of electric relaxation and magnetodielectric effects in rGO–PVA polymer nanocomposites. Scaling of the modulus spectrum shows that the charge transport dynamics is independent of temperature. The small effects in moderate magnetic field are important to decrease of ε', ε''. We have studied graphene (rGO) nanofillers in polymer matrix composite. There are other possible types of composite such as layered (layer by layer assembly) composite of graphene and polymers and the polymer functionalized graphene nanosheets [19]. For search of high magnetodielectric effects all types of graphene–polymer nanocomposites should be investigated.

References

1. A.K. Geim, K. Novoselov, The rise of graphene. Nature Mater **6**, 183–191 (2007)
2. A.K. Geim, Graphene: status and prospects. Science **324**(5934), 1530–1534 (2009)
3. K. Novoselov, V. Fal′ko, L. Colombo et al., A roadmap for graphene. Nature **490**, 192–200 (2012)
4. Y. Zhu, S. Murali, X. Li, J.W. Suk, J.R. Potts, R.S. Ruof, Graphene and graphene oxide: synthesis, properties, and applications. Adv Mater. **22**, 3906–3924 (2010)
5. M.J. Allen, V.C. Tung, R.B. Kaner, Honeycomb carbon: a review of graphene. Chem. Rev. **110**(1), 132–145 (2010)
6. C.N.R. Rao, A.K. Sood, K.S. Subrahmanyam, A. Govindaraj, Graphene: the new two-dimensional nanomaterial. Agnew Chem. Int. Ed. **48**(42), 7752–7777 (2009)
7. S. Vadukumpully, J. Paul, N. Mahanta, S. Valiyaveettil, Flexible conductive graphene/poly(vinyl chloride) composite thin films with high mechanical strength and thermal stability. Carbon **49**(1), 198–205 (2011)
8. J.O. Iroh, J.P. Chime, D.A. Scola, J.P. Wesson, Electrochemical process for preparing continuous graphite fibre-thermoplastic composites. Polymer **35**(6), 1306–1311 (1994)
9. W. Zheng, S.C. Wong, Electrical conductivity and dielectric properties of PMMA/expanded graphite composites. Compos. Sci. Technol. **63**(2), 225–235 (2003)
10. S Ansari, EP Giannelis (2009) Functionalized graphene sheet—Poly(vinylidene fluoride) conductive nanocomposites. J. Polym. Sci. Part B Polym. Phys. **47**(9): 888–897.
11. X.L. Wang, H. Bai, Z.Y. Yao, A.R. Liu, G.Q. Shi, Electrically conductive and mechanically strong biomimetic chitosan/reduced graphene oxide composite films. J. Mater. Chem. **20**(41), 9032–9036 (2010)
12. S. Bose, T. Kuila, M.E. Uddin, N.H. Kim, A.K.T. Lau, J.H. Lee, In-situ synthesis and characterization of electrically conductive polypyrrole/graphene nanocomposites. Polymer **51**(25), 5921–5928 (2010)
13. S. Stankovich, D. Dikin, G. Dommett et al., Graphene-based composite materials. Nature **442**, 282–286 (2006)
14. H. Kim, A.A. Abdala, C.W. Macosko, Graphene/Polymer Nanocomposites. Macromolecules **43**(16), 6515–6530 (2010)
15. J.R. Potts, D.R. Dreyer, C.W. Bielawski, R.S. Ruoff, Graphene-based polymer nanocomposites. Polymer **52**(1), 5–25 (2011)
16. T. Kuilla, S. Bhadra, D. Yao, N.H. Kim, S. Bose, J.H. Lee, Recent advances in graphene based polymer composites. Prog. Polym. Sci. **35**(11), 1350–1375 (2010)
17. D. Cai, M. Song, Recent advance in functionalized graphene/polymer nanocomposites. J. Mater. Chem. **20**(37), 7906–7915 (2010)
18. R. Verdejo, M.M. Bernal, L.J. Romasanta, M.A. Lopez-Manchado, Graphene filled polymer nanocomposites. J. Mater. Chem. **21**(10), 3301–3310 (2011)
19. X. Huang, X. Qi, F. Boey, H. Zhang, Graphene-based composites. Chem. Soc. Rev. **41**(2), 666–686 (2012)
20. R.J. Young, I.A. Kinloch, L. Gong, K.S. Novoselov, The mechanics of graphene nanocomposites: a review. Comp. Sci Technol. **72**(12), 1459–1476 (2012)
21. Z. Li, R.J. Young, N.R. Wilson, I.A. Kinloch, C. Vallés, Z. Li, Effect of the orientation of graphene-based nanoplatelets upon the Young's modulus of nanocomposites. Comp. Sci Technol. **123**, 125–133 (2016)
22. A.J. Marsden, D.G. Papageorgiou, C. Vallés, A. Liscio, V. Palermo, M.A. Bissett, R.J. Young, I.A. Kinloch, Electrical percolation in graphene–polymer composites. 2DMater. **5**(3), 032003 (2018)
23. K. Hu, D.D. Kulkarni, I. Choi, V.V. Tsukruk, Graphene-polymer nanocomposites for structural and functional applications. Prog. Polym. Sci. **39**(11), 1934–1972 (2014)
24. S. Park, R. Ruoff, Chemical methods for the production of graphenes. Nature Nanotech **4**, 217–224 (2009)
25. D.R. Dreyer, S. Park, C.W. Bielawski, R.S. Ruoff, The chemistry of graphene oxide. Chem. Soc. Rev. **39**, 228–240 (2010)
26. K.P. Loh, Q. Bao, P.K. Ang, J. Yang, The chemistry of graphene. J. Mater. Chem. **20**, 2277–2289 (2010)
27. O.C. Compton, S.T. Nguyen, Graphene oxide, highly reduced graphene oxide, and graphene: versatile building blocks for carbon-based material. Small **6**(6), 711–723 (2010)
28. A. Lerf, H. He, M. Forster, J. Klinowski, Structure of graphite oxide revisited. J. Phys. Chem. B **102**(23), 4477–4482 (1998)
29. H. He, J. Klinowski, M. Forster, A. Lerf, A new structural model for graphite oxide. Chem. Phys Lett. **287**(1–2), 53–56 (1998)
30. S. Mitra, O. Mondal, D.R. Saha, A. Datta, S. Banerjee, D. Chakravorty, Magnetodielectric effect in graphene-PVA nanocomposites. J. Phys. Chem. C **115**(29), 14285–14289 (2011)
31. I. Tantis, G.C. Psarras, D. Tasis, Functionalized graphene–poly(vinyl alcohol) nanocomposites: physical and dielectric properties. eXPRESS Polym Lett **6**(4), 283–292 (2012)
32. J.H. Yang, Y.D. Lee, Highly electrically conductive rGO/PVA composites with a network dispersive nanostructure. J. Mater. Chem. **22**(17), 8512–8517 (2012)
33. W.S. Hummers Jr., R.E. Offeman, Preparation of graphitic oxide. j. Am. Chem. Soc. **80**(6), 1339–1339 (1958)
34. N.I. Kovtyukhova, P.J. Ollivier, B.R. Martin, T.E. Mallouk, S.A. Chizhik, E.V. Buzaneva, A.D. Gorchinskiy, Layer-by-layer assembly of ultrathin composite films from micron-sized graphite oxide sheets and polycations. Chem. Mater. **11**(3), 771–778 (1999)
35. H.J. Salavagione, G. Martínez, M.A. Gómez, Synthesis of poly(vinyl alcohol)/reduced graphite oxide nanocomposites with improved thermal and electrical properties. J. Mater. Chem. **19**(28), 5027–5032 (2009)
36. A. Bahrami, I. Kazeminezhad, Y. Abdi, Pt-Ni/rGO counter electrode: electrocatalytic activity for dye-sensitized solar cell. Superlattices Microstruct. **125**, 125–137 (2019)
37. J. Ma, Y. Li, X. Yin, Y. Xu, J. Yue, J. Bao, T. Zhou, Poly(vinyl alcohol)/graphene oxide nanocomposites prepared by in situ polymerization with enhanced mechanical properties and water vapor barrier properties. RSC Adv. **6**, 49448–49458 (2016)
38. J. Ou, J. Wang, S. Liu, B. Mu, J. Ren, H. Wang, S. Yang, Tribology study of reduced graphene oxide sheets on silicon substrate synthesized via covalent assembly. Langmuir **26**(20), 15830–15836 (2010)
39. S.Z. Moghaddam, S. Sabury, F. Sharif, Dispersion of rGO in polymeric matrices by thermodynamically favorable self-assembly of GO at oil–water interfaces. RSC Adv. **4**, 8711–8719 (2014)
40. Y. Xu, W. Hong, H. Bai, C. Li, G. Shi, Strong and ductile poly(vinyl alcohol)/graphene oxide composite films with a layered structure. Carbon **47**(15), 3538–3543 (2009)
41. C. Bao, Y. Guo, L. Song, Y. Hu, Poly(vinyl alcohol) nanocomposites based on graphene and graphite oxide: a comparative investigation of property and mechanism. J. Mater. Chem. **21**(36), 13942–13950 (2011)
42. S. Gahlot, P.P. Sharma, V. Kulshrestha, P.K. Jha, SGO/SPES-based highly conducting polymer electrolyte membranes for fuel cell application. ACS Appl. Mater. Interfaces **6**(8), 5595–5601 (2014)
43. X. Zhao, M. Gnanaseelan, D. Jehnichen, F. Simon, J. Pionteck, Green and facile synthesis of polyaniline/tannic acid/rGO composites for supercapacitor purpose. J. Mater. Sci. **54**, 10809–10824 (2019)

44. L. Shao, J. Li, Y. Zhang, S. Gong, H. Zhang, Y. Wang, The effect of the reduction extent on the performance of graphene/poly(vinyl alcohol) composites. J. Mater. Chem. A **2**(34), 14173–14180 (2014)

45. M. Cano, U. Khan, T. Sainsbury, A. O'Neill, Z. Wang, I.T. McGovern, W.K. Maser, A.M. Benito, J.N. Coleman, Improving the mechanical properties of graphene oxide based materials by covalent attachment of polymer chains. Carbon **52**, 363–371 (2013)

46. H. Beydaghi, M. Javanbakht, E. Kowsari, Synthesis and characterization of poly(vinyl alcohol)/sulfonated graphene oxide nanocomposite membranes for use in proton exchange membrane fuel cells (PEMFCs). Ind. Eng. Chem. Res. **53**(43), 16621–16632 (2014)

47. H.K. Cheng, N.G. Sahoo, Y.P. Tan, Y. Pan, H. Bao, L. Li, S.H. Chan, J. Zhao, Poly(vinyl alcohol) nanocomposites filled with poly(vinyl alcohol)-grafted graphene oxide. ACS Appl. Mater. Interfaces **4**(5), 2387–2394 (2012)

48. Y. Shi, D. Xiong, J. Li, K. Wang, N. Wang, In situ repair of graphene defects and enhancement of its reinforcement effect in polyvinyl alcohol hydrogels. RSC Adv. **7**, 1045–1055 (2017)

49. V.C. Tung, M.J. Allen, Y. Yang, R.B. Kaner, High-throughput solution processing of large-scale graphene. Nat. Nanotechnol. **4**, 25–29 (2009)

50. H. Chen, R. Li, X. Xu, P. Zhao, D.S.H. Wong, X. Chen, S. Chen, X. Yan, Citrate-based fluorophores in polymeric matrix by easy and green in situ synthesis for full-band UV shielding amd emissive transparent disply. J. Mater. Sci. **54**, 1236–1247 (2019)

51. Q. Lai, S. Zhu, X. Luo, M. Zou, S. Huang, Ultraviolet-visible spectroscopy of graphene oxides. AIP Adv. **2**, 032146-1–032146-5 (2012)

52. C.P.P. Wong, C.W. Lai, K.M. Lee, S.B.A. Hamid, Advanced chemical reduction of reduced graphene oxide and its photocatalytic activity in degrading reactive black 5. Materials **8**(10), 7118–7128 (2015)

53. R.M. Abdullah, S.B. Aziz, S.M. Mamand, A.Q. Hassan, S.A. Hussein, M.F.Z. Kadir, Reducing the crystallite size of spherulites in PEO-based polymer nanocomposites mediated by carbon nanodots and Ag nanoparticles. Nanomaterials **9**(6), 874 (2019)

54. S.B. Aziz, M.A. Rasheed, A.M. Hussein, H.M. Ahmed, Fabrication of polymer blend composites based on [PVA-PVP] $(1-x)$:(Ag2S)x $(0.01 \leq x \leq 0.03)$ with small optical band gaps: Structural and optical properties. Mater. Sci. Semiconductor Process 71: 197–203 (2017).

55. S. B. Aziz, Aso Q. Hassan, Sewara J. Mohammed, Wrya O. Karim, M. F. Z. Kadir, H. A. Tajuddin and N. N. M. Y. Chan, Structural and optical characteristics of PVA:C-Dotcomposites: tuning the absorption of ultra violet (UV) region. Nanomaterials **9**, 216 (2019).

56. A.K. Bhunia, T. Kamilya, S. Saha, Temperature dependent and kinetic study of the adsorption of bovine serum albumin to ZnO nanoparticle surfaces. Chem Select **1**(11), 2872–2882 (2016)

57. S.B. Aziz, Modifying Poly(Vinyl Alcohol) (PVA) from insulator to small-bandgap polymer: a novel approach for organic solar cells and optoelectronic devices. J Electron Mater **45**, 736–745 (2016)

58. S.B. Aziz, M.A. Rasheed, H.M. Ahmed, Synthesis of polymer nanocomposites based on [Methyl Cellulose]$_{(1-x)}$:(CuS)$_x$ (0.02 M $\leq x \leq$ 0.08 M) with desired optical band gaps. Polymers, **9**, 194. (2017).

59. M.A. Brza, S.B. Aziz, H. Anuar, M.H.F. Al Hazza, From green remediation to polymer hybridfabrication with improved optical band gaps. Int. J. Mol. Sci. **20**, 3910 (2019)

60. S.B. Aziz, H.M. Ahmed, A.M. Hussein, A.B. Fathulla, R.M. Wsw, R.T. Hussein, Tuning the absorption of ultraviolet spectra and optical parameters of aluminum doped PVA based solid polymer composites. J Mater Sci. **26**(10), 8022–8028 (2015)

61. S.B. Aziz, R.T. Abdulwahid, H.A. Rsaul, H.M. Ahmed, In situ synthesis of CuS nanoparticle with a distinguishable SPR peak in NIR region. J Mater Sci. **27**(5), 4163–4171 (2016)

62. S.B. Aziz, Morphological and optical characteristics of Chitosan$_{(1-x)}$:Cu^o_x ($4 \leq x \leq 12$) based polymer nano-composites: optical dielectric loss as an alternative method for Tauc's model. Nanomaterials **7**, 444 (2017)

63. N.G. McCrum, B.E. Read, G. Williams, *Anelastic and dielectric effects in polymeric solids* (Wiley, New York, 1967)

64. H. Wagner, R. Richert, Thermally stimulated modulus relaxation in polymers: method and interpretation. Polymer **38**(23), 5801–5806 (1997)

65. C. Leon, M.L. Lucia, J. Santamaria, Correlated ion hopping in single-crystal yttria-stabilized zirconia. Phys. Rev. B **55**(2), 882 (1998)

66. R. Richert, H. Wagner, The dielectric modulus: relaxation versus retardation. Solid State Ion. **105**(1–4), 167–173 (1998)

67. P.B. Macedo, C.T. Moynihan, R. Bose, The role of ionic diffusion in polarisation in vitreous ionic conductORS. Phys. Chem. Glasses **13**(6), 171–179 (1972)

68. J. Liu, C.G. Duan, W.G. Yin, W.N. Mei, R.W. Smith, J.R. Hardy, Dielectric permittivity and electric modulus in Bi$_2$Ti$_4$O11. J. Chem. Phys. **119**(5), 2812 (2003)

69. G. Kandhol, H. Wadhwa, S. Chand, S. Mahendia, S. Kumar, Study of dielectric relaxation behaviour of composites of Poly(vinyl alchohol)(PVA) and Reduced grapheme oxide(RGO). Vacuum **160**(02), 384–393 (2019)

70. G. Williams, D.C. Watts, Non-symmetrical dielectric relaxation behaviour arising from a simple empirical decay function. Trans. Faraday Soc. **66**, 80–85 (1970)

71. V. Mydhili, S. Manivannan, Electrical and dielectric behaviour in poly(vinyl alcohol)/poly(3,4-ethylenedioxythiophene):poly(styre nesulfonate) blend for energy storage applications. Polym. Bull. **76**, 4735–4752 (2019)

72. M.M. Parish, P.B. Littlewood, Magnetocapacitance in nonmagnetic composite media. Phys. Rev. Lett. **101**(16), 166602 (2008)

73. G. Catalan, Magnetocapacitance without magnetoelectric coupling. Appl. Phys. Lett. **88**(10), 102902 (2006)

74. X. Xia, J. Hao, Y. Wang, Z. Zhong, G.J. Weng, Theory of electrical conductivity and dielectric permittivity of highly aligned graphene-based nanocomposites. J. Phys. **29**, 205702 (2017)

75. X. Xia, Y. Wang, Z. Zhong, G.J. Weng, A theory of electrical conductivity, dielectric constant, and electromagnetic interference shielding for lightweight graphene composite foams. J. Appl. Phys. **120**, 085102 (2016)

76. J.W. Shang, Y.H. Zhang, L. Yu, B. Shen, F. Lv, P.K. Chu, Fabrication and dielectric propertiesof oriented polyvinylidene fluoride nanocomposites incorporated with graphene nanosheets. Mater. Chem. Phys. **134**(2–3), 867–874 (2012)

77. E.J.G. Santos, E. Kaxiras, Electric-field dependence of the effective dielectric constant in graphene. Nano Lett. **13**(3), 898–902 (2013)

78. S. Sarkar, A. Mondal, K. Dey, R. Ray, Defect driven tailoring of colossal dielectricity of reduced graphene oxide. Mat. Res. Bull. **74**, 465–471 (2016)

79. X. Hong, W. Yu, D.D.L. Chung, Electric permittivity of reduced graphite oxide. Carbon **111**, 182–190 (2017)